Inter-Rotor Spacing Effects on Interactional Aerodynamics and Acoustics of a Coaxial Compound Helicopter in Forward Flight

Sung-U Kang, Si Jin Kim, Kyu-Tae Park, Seong Jin Jo, Rho Shin Myong, Hakjin Lee
School of Mechanical and Aerospace Engineering, Gyeongsang National University, Jinju, South Korea

Abstract

The coaxial rotor is utilized in a high-speed and long-range compound helicopter as its main rotor system, eliminating the need for a tail rotor. To enhance the compound helicopter's survivability, the coaxial rotor system must be designed aerodynamically efficient with low noise. The value of inter-rotor spacing (IRS), which refers to the distance between the upper and lower rotors, is a critical design parameter that determines a coaxial rotor system's aerodynamic and noise performance. This study conducted the computational investigation of the effects of IRS on the interactional aerodynamics and acoustics of the coaxial rotor in low and high-speed forward flight conditions using Spalart-Allmaras detached eddy simulation (SA DES) with the overset mesh technique. When IRS increases, the growth rate of thrust is analyzed to be higher in low-speed conditions than in high-speed conditions, and the fluctuation's amplitude decreases more. Regarding noise, in both conditions, as IRS increases, the impact of loading noise decreases, resulting in a reduction in noise levels.

1. NOTATION[1]

Symbols

R	Rotor radius, m
D	Rotor diameter, m
ψ	Azimuth angle, deg
θ	Elevation angle, deg
α	Shaft tilt angle, deg
μ	Advance ratio
C_nM^2	Normal force coefficient
C_T	Thrust coefficient
σ_{TW}	Total solidity
M_{Tip}	Tip Mach number
IRS	Inter-rotor spacing
OASPL	Overall sound pressure level
DES	Detached Eddy Simulation
FW-H	Ffowcs Williams-Hawkings
MS	Moment area, m^2
BPF	Blade passing frequency
BVI	Blade-vortex interaction
UAM	Urban air mobility

2. INTRODUCTION

The main advantage of a conventional helicopter is its capability to enable vertical takeoff and landing (VTOL) and hover at low altitudes. However, the flight speed, operational range, and transport capacity are limited compared to fixed-wing aircraft. As a result, conventional helicopters cannot achieve high-speed forward flight, which limits their operational range. To overcome the limitations of conventional helicopters, many types of VTOL rotorcraft utilizing different rotor configurations have attracted much attention. Bell developed the V-280 Valor with tilt rotors to enable control over flight direction. Piasecki developed the X-49 SpeedHawk, which features a ducted fan at the fuselage's rear side to enhance the pusher propeller's thrust efficiency. X^3 is a compound helicopter developed by Eurocopter, equipped with two tractor propellers mounted on the fuselage wings, allowing it to fly at high speeds. Sikorsky-Boeing developed the SB>1 defiant, which utilizes a coaxial counter-rotating rotor system for the main rotor to increase thrust. Among various rotor systems, the coaxial rotor enhances helicopter stability and maneuverability by eliminating the need for a tail rotor, as the counter-rotating blades naturally cancel out torque. This design also allows for greater lift capacity and compactness, making it ideal for operations in confined spaces. For these reasons, the coaxial rotor is widely used for next-generation high-speed and long-range compound helicopters (Ref. 1), urban air mobility (UAM) (Refs. 2-3), and drones.

The coaxial counter-rotating rotor configuration is useful for generating about 1.7 times additional thrust in the limited space by making the upper and lower rotors rotate in opposite directions to counterbalance the torque (Ref. 4). It removes the need for a tail rotor, saving on the weight and power consumption required to operate it. This creates space for the installation of auxiliary propellers, which give rotorcrafts additional propulsive force and enable high-speed flight (Ref. 5). However, the mutual interaction between the upper and lower rotors causes complex flow interference, which could significantly decrease aerodynamic performance and increase noise levels compared to conventional helicopters with single main rotor system. Moreover, rotor-wake interaction complicates the understanding of the physical phenomena occurring in coaxial helicopters. The interaction between the two vertically arranged rotors is of critical importance. The inter-rotor spacing (IRS) refers to the distance between the upper and lower rotors, and it serves as a key parameter in controlling the interaction effects in coaxial helicopters. The large IRS reduces the interactional aerodynamics between the upper and lower rotor, but the bulky hub design that comes along with it generates a significant parasite drag. On the other hand, as the IRS decreases, the aerodynamic interaction between the upper and lower rotors increases, even if the performance loss brought on by parasite drag decreases. Therefore, more vibrations during flight may make it difficult to control and raise noise levels.

Ramasamy (Ref. 6) investigated the interactions between the IRS and interference loss factor in hovering conditions. Wake interactions may cause wake instability in hovering conditions, leading to asymmetry and aperiodicity. Wake instability impacts the distribution of unsteady loading and wake-induced inflow. It is essential to predict unsteady loads in aerodynamics correctly (Ref. 7) and aeroacoustics (Ref. 8). Leishman and Anathan (Ref. 9) developed the blade element momentum theory (BEMT) model for the coaxial rotor to design the optimal coaxial rotor. Also, Lee and Dassonville (Ref. 10) developed a new BEMT for a coaxial rotor, indicating each rotor's aerodynamic performance in relation to the IRS in hover. Harrington's data (Ref. 11), which provides experimental data about the thrust to power coefficients at a given distance, was used to validate these BEMT models. Leishman and Syal (Ref. 12) used momentum theory and the Harrington data to develop the figure of merit formulas for a coaxial rotor considering four different operating conditions. Ho et al. (Ref. 13) used Harrington and Ramasamy data to investigate coaxial rotor performance in hover and forward flight using RCAS SW. The impact of rotor-wake interference on the wake geometry and performance of a coaxial rotor was investigated by Nagashima and Nakanishi (Ref. 14) using the momentum equation and a simplified free wake analysis. Ko and Lee (Ref. 15) investigated the wake structure of a coaxial rotor when IRS changes, indicating that the low IRS makes blade-vortex interaction (BVI) stronger than high IRS. Qi et al. (Ref. 16) investigated the thrust fluctuation of a coaxial rotor, showing the overlap effect generated by the bound vortices of both rotors and the induction effect caused by the wake interaction. Park and Kwon (Ref. 17) analyzed the IRS effects on aerodynamic performance of the isolated coaxial rotor in hover and forward flight.

Most research has analyzed the IRS effects on aerodynamics and aeroacoustics on the isolated rotor configuration. However, wakes from a coaxial helicopter's upper and lower rotors could interfere with the fuselage and blades in forward flight, affecting the noise and aerodynamics. Thus, based on the forward flight speed of a coaxial rotor helicopter, it is necessary to investigate the IRS effects on the helicopter's noise and aerodynamics. The Spalart-Allmaras detached eddy simulation (SA-DES) is performed to compute the aerodynamic loading acting on the coaxial rotor blades and capture complex wake flow (Ref. 18). The overset mesh technique is adopted to carry out the coaxial rotor's trim analysis in forward flight conditions (Ref. 19). Based on the results of aerodynamic analysis, thickness noise, and loading noise, which exhibit periodic characteristics associated with blade passing frequency (BPF), were evaluated using the acoustic analogy method with the Farassat 1A formulation. The DES predictions are compared against the Harrington rotor 1 model's experimental results and the X2TD rotor's other computational results for validation work. Finally, the full configuration of the high-speed and long-range compound helicopter X2TD, equipped with a coaxial rotor, is employed to investigate the interactional aerodynamics and acoustics in forward flights.

3. Numerical Methodology

3.1. Aerodynamic Analysis Method

This study employed the detached eddy simulation (DES) equation to analyze the aerodynamic and acoustic characteristics of a compound helicopter equipped with coaxial contra-rotating rotors. The DES is a hybrid approach that combines features of the Reynolds-averaged Navier-Stokes (RANS) and the large eddy simulation (LES). DES turbulence models solve the boundary layers and irrotational flow regions using a base RANS approach. However, when the grid is sufficiently fine, it emulates an LES subgrid-scale model in areas of detached flow. This allows for using RANS in boundary layers and LES in unsteady separated regions, producing the advantages of both techniques. Turbulence models in RANS can be divided into Spalart-Allmaras DES, Elliptic Blending k-ε DES, and Shear Stress Transport (SST) k-ω DES. This study used the Spalart-Allmaras turbulence model due to its ability to analyze large and complex flow fields with a lower computational cost and high accuracy in turbulence analysis near wall surfaces (Ref. 20).

The mean velocity $\bar{v}$ from RANS and the filtered velocity $\tilde{v}$ from LES can be expressed by Eq. (1) and (2), respectively, in the momentum equations.

$$\frac{\partial}{\partial t}(\rho\bar{\mathbf{v}}) + \nabla\cdot(\rho\bar{\mathbf{v}}\otimes\bar{\mathbf{v}}) = -\nabla\cdot\bar{p}\mathbf{I} + \nabla\cdot(\bar{\mathbf{T}} + \mathbf{T}_{\mathbf{RANS}}) + \mathbf{f_b} \tag{1}$$

$$\frac{\partial}{\partial t}(\rho\tilde{\mathbf{v}}) + \nabla\cdot(\rho\tilde{\mathbf{v}}\otimes\tilde{\mathbf{v}}) = -\nabla\cdot\tilde{p}\mathbf{I} + \nabla\cdot(\tilde{\mathbf{T}} + \mathbf{T}_{\mathbf{RANS}}) + \mathbf{f_b} \tag{2}$$

The Reynolds Stress Tensor ($\mathbf{T}_{\mathbf{RANS}}$) is defined as a function of time and length scales in Eq. (3), and it is represented by Eq. (4) for LES.

$$\mathbf{T}_{\mathbf{RANS}} = f(\nabla\cdot\bar{\mathbf{v}}, \mathrm{k}, \varepsilon) \tag{3}$$

$$\mathbf{T}_{\mathbf{SGS}} = f(\nabla\cdot\tilde{\mathbf{v}}, \Delta) \tag{4}$$

In Eq. (4), the width of the filter and the length scale are the most important factors. These are used not only for the definition of subgrid-scale eddy viscosity but also in many models for the transition region. The similarities in Eq. (1) and (2) allow for a unified approach to be used to solve for a quantity $\hat{u}_i$ as represented in Eq. (5).

$$\frac{\partial}{\partial t}(\rho\hat{\mathbf{v}}) + \nabla\cdot(\rho\hat{\mathbf{v}}\otimes\hat{\mathbf{v}}) = -\nabla\cdot\hat{p}\mathbf{I} + \nabla\cdot(\hat{\mathbf{T}} + \mathbf{T}_{\mathbf{RANS}}) + \mathbf{f_b} \tag{5}$$

And the model $\mathbf{T}_{\mathbf{RANS}}$ is defined by Eq. (6).

$$\mathbf{T}_{\mathbf{model}} = \mathrm{f}_{\triangle}(\frac{\triangle}{\mathrm{l_k}})\mathbf{T}_{\mathbf{RANS}} \tag{6}$$

For unsteady simulations, time advancement is accomplished by the dual time stepping technique, with 15 sub-iterations per time step and a time step of 1° per rotor blade rotation angle. Using Roe's Flux-Difference Splitting Scheme (FDS), inviscid flux evaluation is employed, and spatial accuracy is acquired through the MUSCL-3rd order scheme. Venkatakrishnan's flux limiter reduces numerical oscillations caused by shock waves on the advancing rotor blade faces during forward flight.

3.2. Aeroacoustic Analysis Method

This study employed the Farassat 1A formula, based on the theoretical solution of the FW-H, to predict the noise generated by the coaxial rotor helicopter when it's moving (Ref. 21). The fluid movement during blade rotation is the source of thickness noise. Aerodynamic forces operating on the blade surfaces cause loading noise, and interference between the rotating blade and strong tip vortices developed at the blade ends is the source of blade vortex interaction (BVI) noise. Also, high-speed impulsive (HSI) noise occurs at the rotor blades' advancing side (Ref. 22). In cases where coaxial rotor is used, interference between the upper and lower rotors may create interactional noise, which can then affect the loading noise.

The thickness noise and loading noise caused by the surfaces of the coaxial rotor blades were analyzed using the acoustic analogy with impermeable boundary conditions. Eq. (7) shows the Farassat 1A formulation that contains the acoustic pressure from the thickness noise source p'_T and the loading noise source p'_L.

This formulation was used to calculate the magnitude of each type of noise that moved to the observer's position. Eq. (8) and Eq. (9) indicate each noise source's acoustic pressure specifically, and the values in brackets are calculated at a retarded time(Ref. 23).

(7) $$p'(x,t) = p'_T(x,t) + p'_L(x,t)$$

(8) $$p'_T(x,t) = \frac{1}{4\pi}\int_{f=0}\left[\frac{\rho_0(\dot{\upsilon}_n + \upsilon_{\dot{n}})}{r\left|1-M_r\right|^2}\right]dS + \frac{1}{4\pi}\int_{f=0}\left[\frac{\rho_0\upsilon_n(r\dot{M}_r + a_0M_r - a_0M^2)}{r^2\left|1-M_r\right|^3}\right]_{ret} dS$$

(9) $$p'_T(x,t) = \frac{1}{4\pi a_0}\int_{f=0}\left[\frac{\dot{l}_r}{r\left|1-M_r\right|^2}\right]_{ret} dS + \frac{1}{4\pi}\int_{f=0}\left[\frac{l_r - l_M}{r^2\left|1-M_r\right|^2}\right]_{ret} dS + \frac{1}{4\pi a_0}\int_{f=0}\left[\frac{l_r(r\dot{M}_r + a_0M_r - a_0M^2)}{r^2\left|1-M_r\right|^3}\right]_{ret} dS$$

A spatial delay is equal to the time required for the sound wave to move through the spatial distance between the noise source and the observer. As a result, the point at which sound is generated at the source is transmitted to the observer much later. Eq. (10) and Eq. (11) show the spatial distance, and Eq. (12) indicates the delay time between the noise source and the observer.

(10) $$r = \left|x_i - y_i\right|$$

(11) $$\hat{r}_i = \frac{x_i - y_i}{r}$$

(12) $$\tau = t - \frac{r}{a_0}$$

4. Numerical Setup

4.1. Compound Helicopter Model

The Sikorsky X2TD rotor blades and fuselage were used to analyze the IRS and advance ratio effects on the aerodynamics and acoustics in forward flight conditions. Table 1 shows the geometric information of X2TD helicopter, referred from Passe et al. (Ref. 24). Each rotor has four blades, for a total of two rotors, and each blade has a radius of 4.023 m. The upper rotor and lower rotor rotate counter-clockwise and clockwise, respectively. The planform, twist angle, and thickness distribution of the X2TD rotor blade spanwise are shown in Figure 1 (Ref. 25). From available data and engineering estimates, generic airfoil profiles at important span locations were derived (Ref. 26). With the use of two elliptic parts, the X2 main rotor blade is designed to reduce the considerable drag that the inboard sections encounter when operating in reverse flow. A transonic airfoil is used at the tip to minimize compressibility drag, transitioning from a sharp trailing edge high-lift cross-section at the mid-span. These data were used to choose template cross-section profiles for the X2TD main rotor blades, assuming that the upper and lower rotors would have the same configurations. The template airfoil cross-sections were slightly modified for improved smoothness throughout the blade surface to ensure that the blade geometry aligned as closely as possible with the available data. These modifications are shown in Table 2 (Ref. 24). From the blade spanwise of 0.142R to 0.331R, which R is the radius of the rotor, the elliptical airfoil DBLN-5262 airfoil was employed. From 0.468R to 0.568R, the SC1012-R8 airfoil was used, and from 0.6R to the tip, the SSCA-09 airfoil was used.

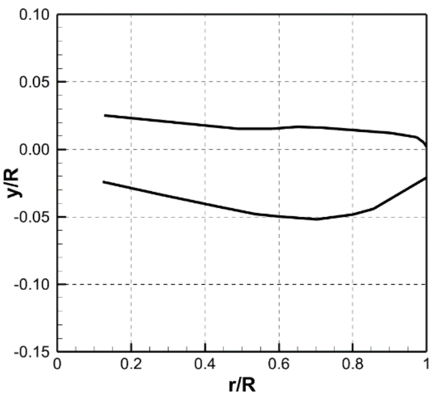

(a) Blade planform

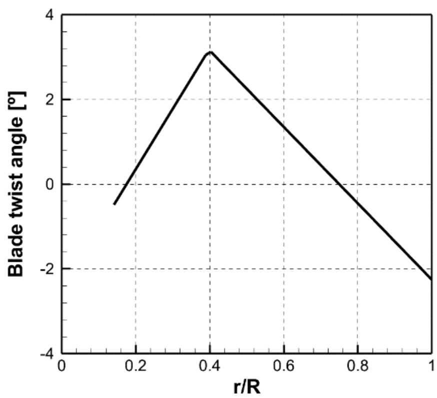

(b) Blade twist angle

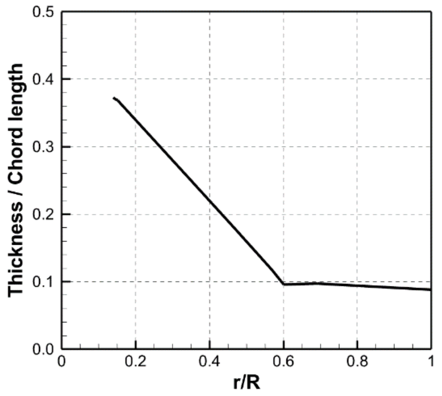

(c) Blade thickness

Figure 1: Blade information of X2TD rotor

Table 1: Geometry of X2TD helicopter (Ref. 24)

Properties	Specification
Gross Weight [kg]	2,700
Radius, R [m]	4.023
Number of Rotors, N_b	2
Blades per Rotor	4
Total Solidity, σ_{TW}	0.14
Rotation Direction	CCW Upper rotor
Blade Aspect Ratio	19.2
Tip Mach Number, M_{Tip}	0.556
Rotor Vertical Separation [m]	0.443
Fuselage Length [m]	9.1
Horizontal Tail Area [m^2]	3.159

Table 2: Airfoil cross sections of X2 rotor blade (Ref. 24)

Radial Location (r/R)	Template Airfoil Section
0.142	DBLN-526
0.331	DBLN-526
0.468	SC1012-R8
0.568	SC1012-R8
0.600	SSCA-09
1.000	SSCA-09

4.2. Grid System and Boundary Condition

To investigate the IRS effects on the aerodynamics of the helicopter, the computational domains and grid system for SA-DES are depicted in Figure 2 and Figure 3. And grid distribution around the blades and their surroundings is illustrated in Figure 4. The size of computational domain is 10D (W) x 10D (H) x 20D(L). Here D is the rotor diameter. The minimum mesh size is 5 mm, corresponding to 2% of the chord length at 75% of the spanwise. The rotor blade's pitching motions are considered using the overset mesh technique. 76 million grids are used for computational analysis, including 4 million in the area near each blade and 3 million in the fuselage. The no-slip boundary condition is imposed on the surfaces of the compound helicopter, and velocity inlet and pressure outlet boundary conditions are applied to the surfaces of the computational domain.

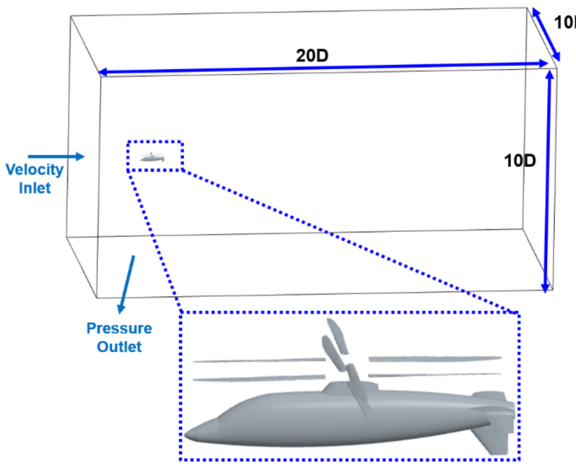

Figure 2: Computational domain for simulating X2TD helicopter in full configuration at forward flight condition

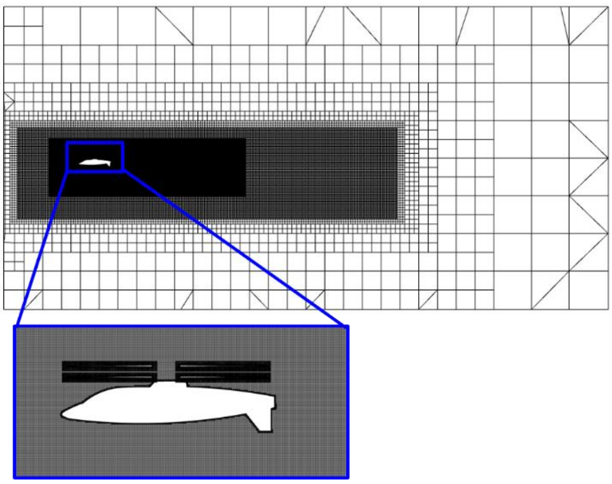

Figure 3: Computational grid system for SA-DES

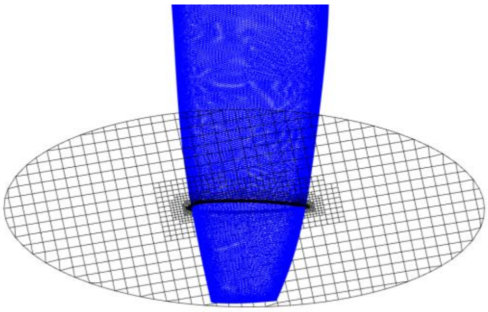

Figure 4: The surface grid of the rotor blade

The forward flight conditions for the IRS and advance ratio effects on the aerodynamics and aeroacoustics in forward flight in this study are presented in Table 3. X2TD helicopter is operated in forward flight conditions by employing atmospheric conditions at 4,000 ft. The rotor's original vertical separation is 0.443 m or 0.055D. To investigate how IRS changes affect the X2TD helicopter's noise and aerodynamics, cases with IRS values of 0.055, 0.0825, and 0.11 were considered. The helicopter's advance ratios were set for 0.15 and 0.41 to investigate the IRS effects on aerodynamics and noise in low and high-speed flight conditions. Six rotor revolutions of computational analysis are conducted to ensure sufficient frequency resolution (Δf). After two revolutions, the aerodynamic data from the helicopter converged adequately. Therefore, data obtained after the second rotation is used in the analysis. Using parallel computing and an Intel(R) Xeon(R) Gold 6230R CPU operating at 2.1 GHz and 128 cores, the computational analysis for five rotations of an isolated rotor was done in approximately 32 hours.

Table 3: Forward flight simulation information

Properties	Specification
IRS (H/D)	0.055, 0.083, 0.11
Advance Ratio	0.15, 0.41
Reynolds Number	2.5 x 10^6
Flight Altitude	4,000 ft
Pressure	87,494 Pa
Temperature	280.21 K

The upper and lower rotor's pitch angle coefficients for each advance ratio were calculated by trimming the collective and cyclic pitch angles until the target air load was reached, using prior research as a reference. Table 4 displays the pitch angles used in this study (Ref. 24).

Table 4: Pitch angle conditions of each advance ratio (Ref. 24)

Advance Ratio (μ)	Pitch angle	Upper Rotor's Value [°]	Lower Rotor's Value [°]
0.15	θ_0	9.45	9.39
	θ_{1c}	3.29	3.29
	θ_{1s}	-3.65	3.16
	α	-0.44	-0.44
0.41	θ_0	5.95	6.08
	θ_{1c}	0.28	0.28
	θ_{1s}	-5.90	5.93
	α	2.10	2.10

4.3. Microphone Setup

24 microphones were positioned at intervals of 15° around the rotational axis of the lower rotor blade at a distance of 40.23 m, 10 times the rotor radius (R), to predict the noise variations due to changes in IRS and advance ratio. Figure 5 illustrates the distribution of the microphones for noise analysis according to azimuth and elevation angles.

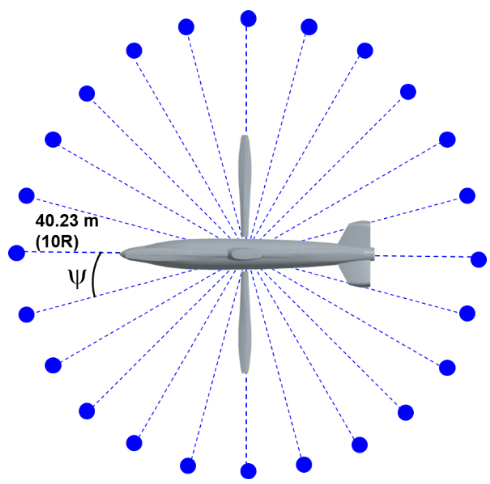

(a) Azimuth angle

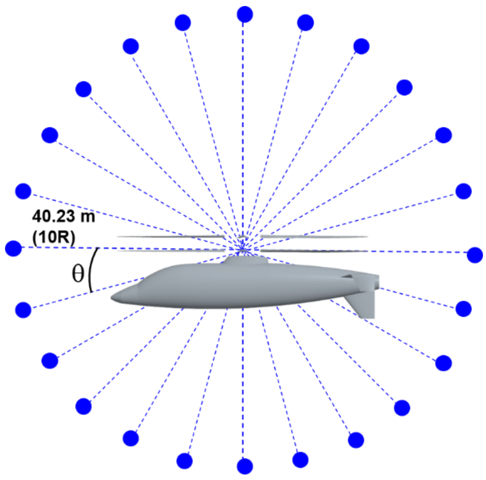

(b) Elevation angle

Figure 5: Microphone array

5. Numerical Results

5.1. Validation

The numerical validation was carried out before analyzing a compound helicopter's aerodynamic and noise characteristics due to changes to the IRS and advance ratio. The thrust and power of the Harrington rotor 1 model with respect to advance ratio were evaluated using SA-DES, and the predictions were compared to the experimental results for validation work (Ref.11). The blade planform of the Harrington rotor 1 is shown in Figure 6. It has a taper ratio of 0.39 and is composed of six different kinds of symmetrical airfoils without a twist angle.

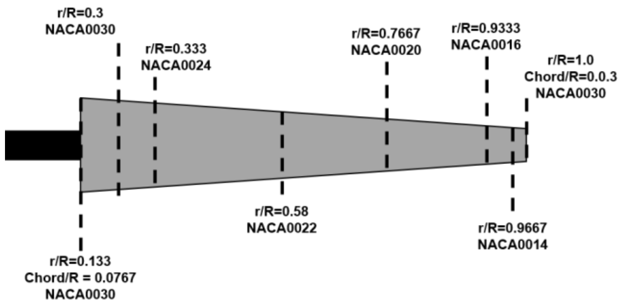

Figure 6: Blade planform of Harrington rotor 1

Cyclic pitch angles for the upper and lower rotors during the forward flight to get the target thrust on the advance ratio were referred to in the previous study (Ref. 27). Experimental data for the Harrington rotor 1 measured the power on advance ratio, which is from 0.12 to 0.24, with increments of 0.02, when the thrust coefficient was 0.0047. Compared with the data, when using SA-DES, thrust on the advance ratio of Harrington rotor 1 showed an error within 4%. The power comparison shown in Figure 7 illustrates the SA-DES predictions are in excellent agreement with the experimental data within the maximum prediction error of 3.5%.

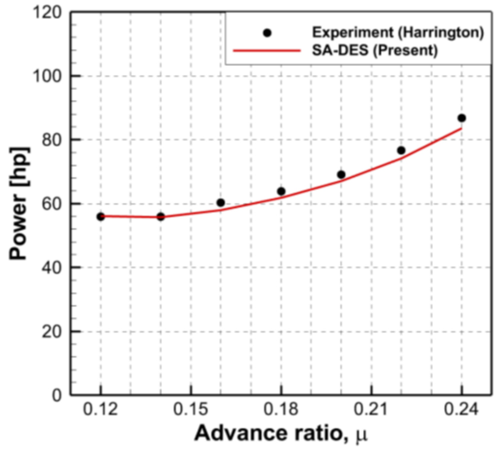

Figure 7: Comparison of power of the Harrington rotor 1 with the experiment on advance ratio

This study investigated the thrust produced by an isolated coaxial rotor at an advance ratio of 0.15 in low-speed flight conditions with various mesh counts to confirm the mesh density used for the computational analysis of the X2TD rotor. Table 4 shows the thrust generated by the rotor on the number of cells with the total computation time. Thrust was investigated and compared for the resolution test in four cases, ranging in total cell counts from 44 million to 74 million. The thrust grew as the total number of cells increased. Particularly, case employing 60 million cells increased thrust by about 2% compared to case of 54 million cells. Compared to the case using 60 million cells, thrust increased by about 0.4% when 74 million cells were used, and computation time increased by six hours. Thus, considering the computational time and thrust, a case with 60 million cells is chosen, providing accurate thrust at less computational cost than the case with 74 million cells.

Table 4: Grid convergence test results of X2TD isolated rotor

Total cells	Time	Thrust [N]
44 mil.	18 hrs.	26,900
54 mil.	26 hrs.	27,100
60 mil.	30 hrs.	27,500
74 mil.	36 hrs.	27,600

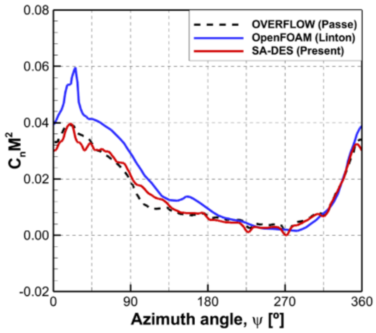

(a) Upper rotor at chord position of 0.30R

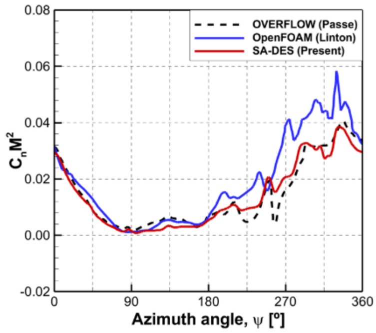

(b) Lower rotor at chord position of 0.30R

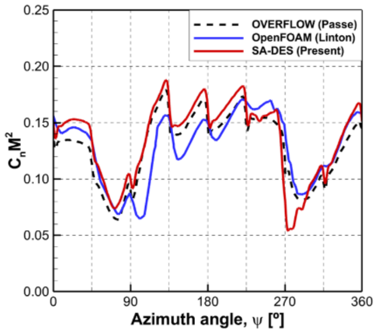

(c) Upper rotor at chord position of 0.85R

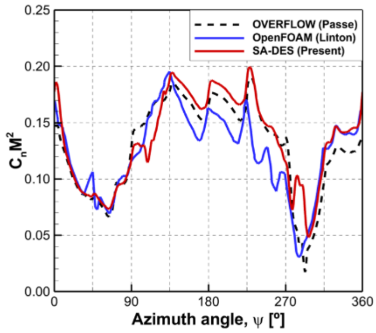

(d) Lower rotor at chord position of 0.85R

Figure 8: Sectional normal force coefficient in μ=0.15

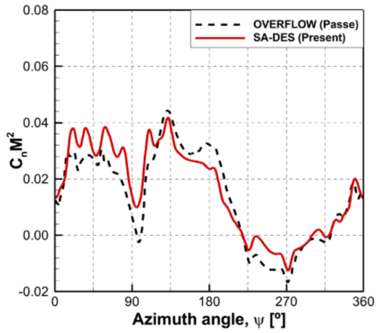

(a) Upper rotor at chord position of 0.30R

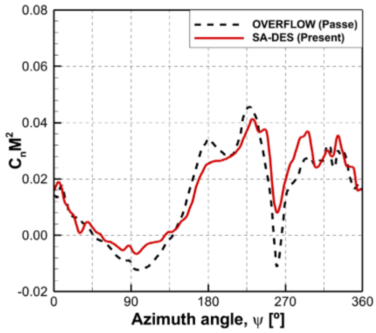

(b) Lower rotor at chord position of 0.30R

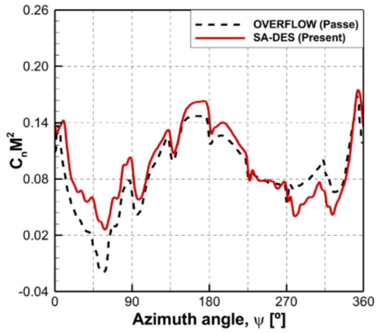

(c) Upper rotor at chord position of 0.85R

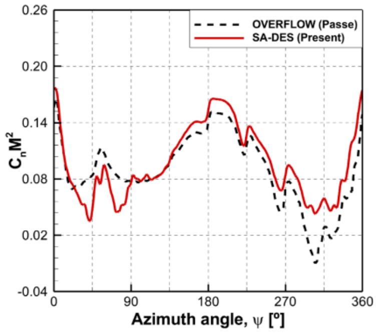

(d) Lower rotor at chord position of 0.85R

Figure 9: Sectional normal force coefficient in μ=0.41

The sectional normal forces generated by the upper and lower rotor blades were compared with the other computational results to validate the aerodynamic performance of the X2TD isolated coaxial rotor (Ref. 24). Another solver's investigation of the sectional normal force in slow-speed flight conditions was compared to perform additional comparisons with the other computational results (Ref. 28). Figure 8 and

Figure 9 show the normal force coefficients investigated at chords located at 0.3R and 0.85R in the spanwise of the blades for advance ratios of 0.15 and 0.41 which are the low and high-speed flight conditions. The azimuth angle is opposite for the blade positions for the lower rotor, rotating clockwise, and the upper rotor rotating counterclockwise. The absolute azimuth angle was set when rotating counterclockwise, standardizing it for both rotors to prevent confusion caused by the differences. The sectional forces investigated at chord locations of 0.30R and 0.85R were analyzed closely compared to the other results using OpenFOAM and OVERFLOW. Additionally, when the lower rotor blade faced the advancing side, a rapid increase in normal force was accurately predicted at the 0.85R chord position.

The low-speed flight conditions were validated by comparing the normal force on the azimuth angle with the other computational results. Based on the validation, OVERFLOW's investigation of the results and the normal forces created by the upper and lower rotor blades at an advance ratio of 0.41 in high-speed flight conditions were compared. The OVERFLOW results indicated small differences at the 0.85R chord position, where the lower rotor passes the retreating side, and the upper rotor passes the advancing side from 270°°to 360°. On the other hand, other regions generated similar predictions about the normal forces. This validation confirms that employing the SA-DES model to investigate the IRS effects on aerodynamics and noise for the X2TD helicopter is appropriate.

5.2. IRS Effects on Aerodynamics in Low-Speed Conditions

This study investigated the IRS effects on the coaxial rotor helicopter's aerodynamics when the advance ratio is 0.15 in low-speed flight conditions. The thrust generated at the upper and lower rotors as the IRS increases is displayed in Figure 10, and Table 5 presents the averaged thrust coefficient. The thrust fluctuation of the upper and lower rotors is 8/rev, indicating that for one revolution, the rotor blade passes the other eight times. The interference scale between the upper and lower rotor diminished as the IRS increased, improving thrust. There is a tendency to absorb the flow beneath the upper rotor, mainly when the lower rotor rotates. This reduces the pressure difference between the lower and upper surface of the upper rotor so that the thrust decreases. However, when the IRS increases, the flow absorption from the upper to the lower rotor weakens, and the upper rotor's thrust increases. Also, the lower rotor's thrust dropped less when the blades crossed the lower rotor, with a spacing of 45°° This is because the wake created by the upper rotor interacted with the lower rotor less than IRS is small. This leads to generating the additional thrust at the lower rotor.

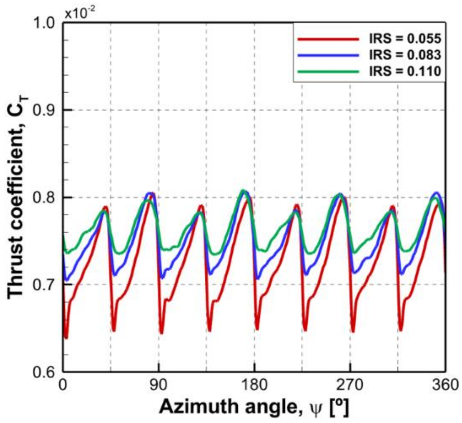

(a) Upper rotor (CCW)

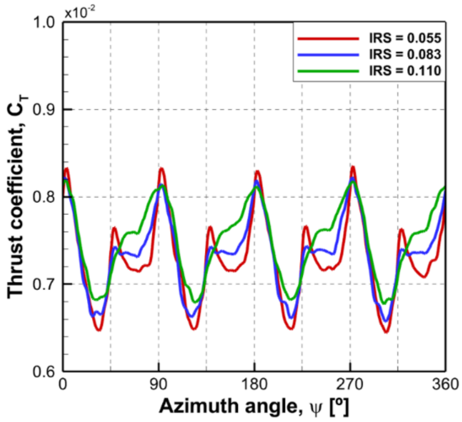

(b) Lower rotor (CW)

Figure 10: Thrust coefficient on azimuth angle in low-speed flight condition

Table 5: Averaged thrust coefficient depending on IRS at μ=0.15 condition

IRS	0.055	0.083	0.110
Upper rotor	0.00727	0.00752	0.00763
Lower rotor	0.00729	0.00735	0.00750
Total rotors	0.01460	0.01487	0.01513

Investigating the normal force on the blade's spanwise is essential because the IRS increased the upper and lower rotor's thrust. Figure 11 illustrates how the IRS affects the normal force along the spanwise of the upper and lower rotor blades in low-speed flight conditions. Using the DBLN-526 airfoil, the normal force hardly changed before the chord position of 0.331R, while the IRS increased. However, significant differences in normal force were observed when using SC1012-R8 and SSCA-09 airfoils after the chord position of 0.468R. The upper rotor's normal force improved as the IRS increased, especially as the chord position moved close to the tip. This is because the large IRS reduces the flow absorption force at the lower rotor, increasing the pressure difference between the upper rotor's lower and upper blade surfaces. When the IRS increased, the lower rotor interacted with less downwash from the wake created by the upper rotor, and the inflow angle at the blade tip decreased, increasing normal force. The case with the small IRS generates more normal force than the large IRS, especially before the chord position of 0.85R, but creates less force over that position. Because the difference in the upper rotor's normal force is maximum on the IRS, it is necessary to analyze the normal forces at the chord position at 0.85R on the azimuth angle.

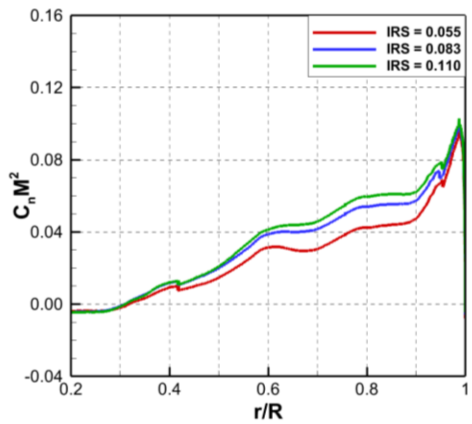

(a) Upper rotor (CCW)

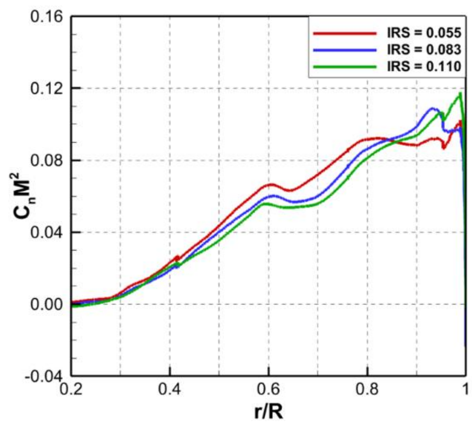

(b) Lower rotor (CW)

Figure 11: Normal force coefficient of rotor blade on spanwise in low-speed flight condition

The IRS effect on the normal force at a chord position of 0.85R in low-speed conditions is shown in Figure 12. The difference in the normal force is the most visible at the azimuth angle of 90° and 270°, where the upper and lower rotor blades pass through the advancing and retreating sides. Increased IRS improves the pressure difference between the blade's upper and lower surface at the upper rotor with a high relative speed, generating additional normal force. In contrast, a small difference of normal force occurred on the retreating side due to stalling, in which the angle of attack is high, and the relative speed is slow. Strong downwash generated from the advancing side and significant flow separation on the upper rotor's retreating side rarely affect the lower rotor blades when the IRS increases, so that increases the normal force.

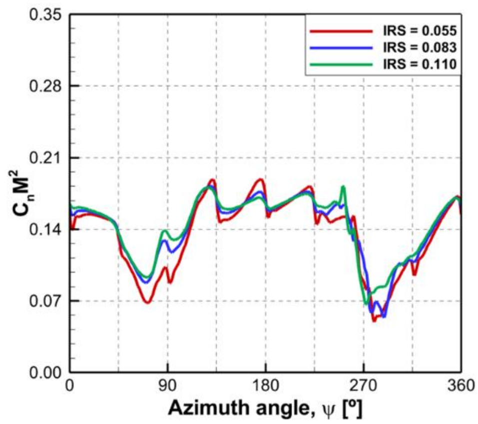

(a) Upper rotor (CCW)

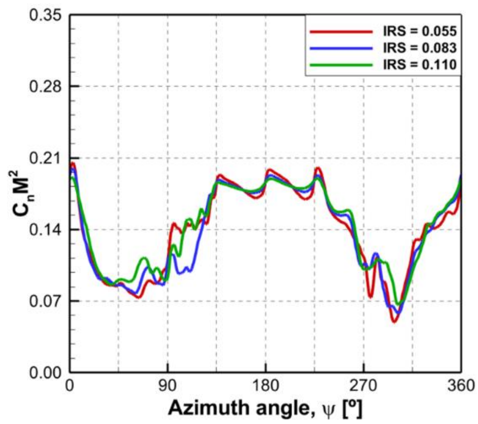

(b) Lower rotor (CW)

Figure 12: Sectional normal force coefficient on azimuth angle at r/R=0.85 in low-speed flight condition

The IRS grew as the upper and lower rotor thrust increased in low-speed flight conditions. This occurs due to changes in the flow around the X2TD helicopter, so an investigation of the IRS effect on wake characteristics is required. Figure 13 demonstrates the IRS effects on the wake structures of a coaxial rotor helicopter employing Q-criterion Iso-surfaces. The rotor blades at the smallest IRS in Figure 13(a) generate significant rolled-up tip vortices due to interference between the upper and lower rotors. At this point, the rotor blades' advancing and retreating sides exhibit super-vortices with strong vorticity. Also, due to the interference between the wakes created by the two rotors, unstable flows propagate to the rear. As the IRS increases, the interference displayed in Figure 13(b) and Figure 13(c) decreases. More steady flow may propagate over a wider area because it weakens the tip vorticity at the rotor blades' advancing and retreating sides and reduces the interference between wakes at the back.

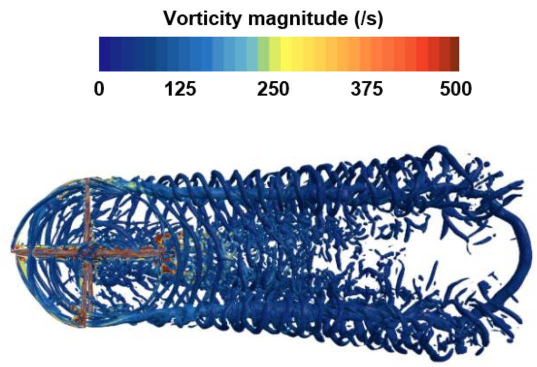

(a) IRS = 0.055

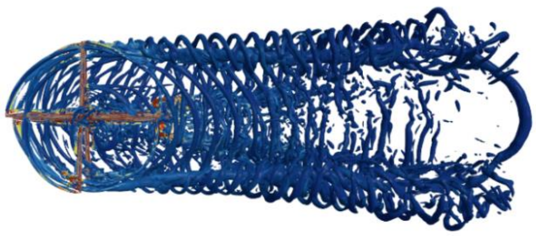

(b) IRS = 0.083

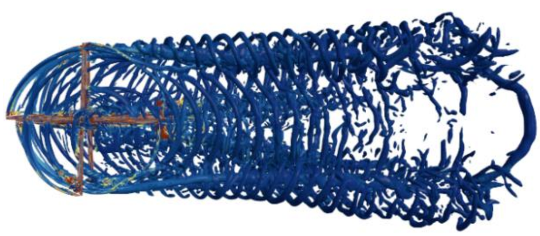

(c) IRS = 0.110

Figure 13: Wake structures represented by an iso-surface of Q-criterion colored by vorticity magnitude in low-speed flight condition

Figure 14 illustrates the IRS effects on the flow around the X2TD helicopter in low-speed flight conditions by modeling the sectional vortex fields. Strong vorticity is created when the wake from the upper and lower rotors intersect, as seen in Figure 14(a). These wake then interfere with the fuselage, especially at the horizontal stabilizer. This occurrence gets weakened, and the wake's vorticity decreases when the IRS gets larger in Figure 14(b) and Figure 14(c). The interference between the rotors' wake and the fuselage could impact the helicopter's aerodynamics and maneuverability, so it is essential to analyze the IRS effect on the fuselage's pitching moment.

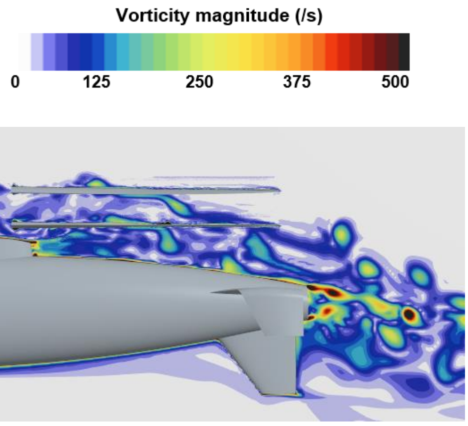

(a) IRS = 0.055

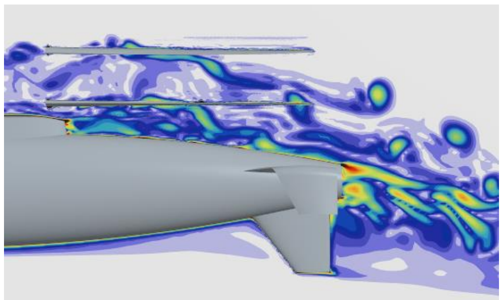

(b) IRS = 0.083

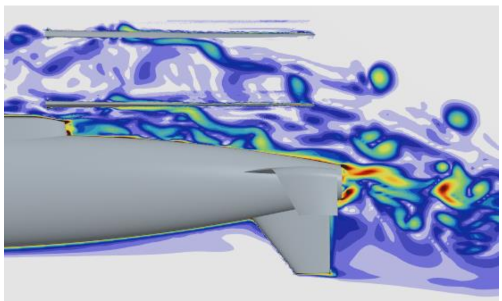

(c) IRS = 0.110

Figure 14: Vorticity contours around X2TD helicopter with IRS effect in low-speed flight condition

To investigate the interference between the wake created by the rotors and the fuselage, Figure 15 displays the IRS effects on the fuselage's pitching moment in low-speed conditions. The fluctuations show 8/rev that each rotor passes the fuselage four times for a revolution. But when the IRS increases, the wake created by the upper rotor rarely interferes with the fuselage. So, when looking at the case of IRS=0.110, the fluctuation's amplitude at the 2nd, 4th, 6th, and 8th are reduced. Also, the interference between the lower rotor and the fuselage decreases as IRS increases because the wakes from the upper and lower rotors have less vorticity. The advancement of stability indicates that as IRS increases, the coaxial helicopter's maneuverability improves.

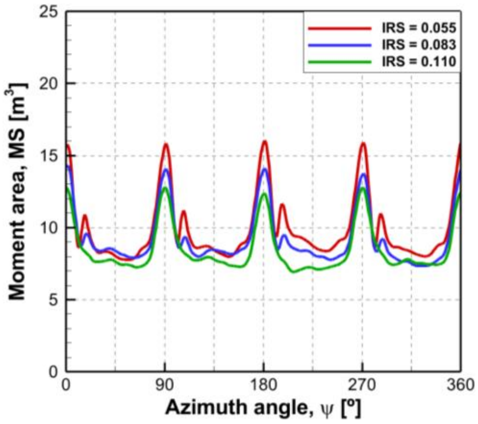

Figure 15: Moment area of the fuselage at IRS effect on azimuth angle in low-speed flight condition

5.3. IRS Effects on Aerodynamics in High-Speed Conditions

The IRS effects on the aerodynamics and flow around the helicopter were analyzed in low-speed flight conditions. Likewise, to investigate the IRS effects in high-speed flight conditions, the advance ratio is set to be 0.41. Figure 16 illustrates the IRS effects on the thrust in high-speed flight conditions. Table 6 shows the average thrust coefficient per revolution for the upper and lower rotors, compared to the results from low-speed flight conditions demonstrated in Table 7. In high-speed flight conditions, compared to low-speed flight conditions, the reduction rate in thrust fluctuation's amplitude is lower when the separation distance of the upper and lower rotor increases. As a result, in low-speed flight conditions, the thrust generated by the upper and lower rotors increases by up to 3.63% as the IRS increases. In contrast, only an additional 0.71% of thrust is created in high-speed flight conditions. This is because the wake created by the upper rotor propagates faster, even with a smaller IRS, causing less interference with the lower rotor.

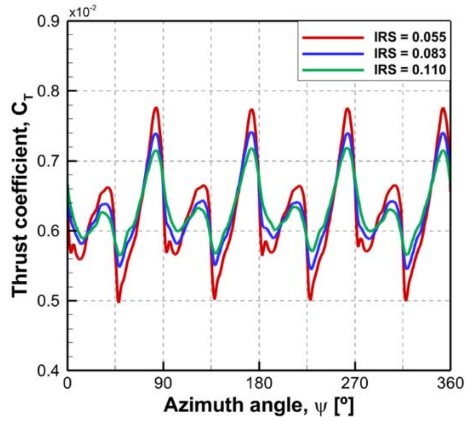

(a) Upper rotor (CCW)

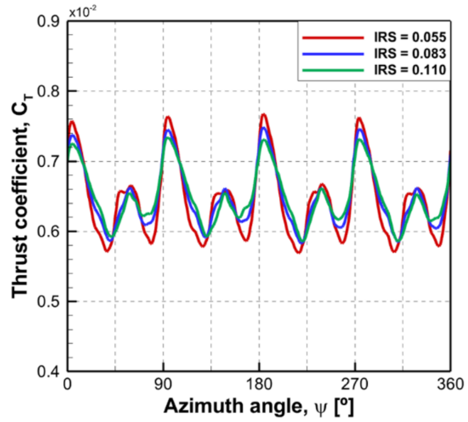

(b) Lower rotor (CW)

Figure 16: Thrust coefficient on azimuth angle in high-speed flight condition

Table 6: Averaged thrust coefficient on IRS in high-speed flight condition

IRS	0.055	0.083	0.110
Upper rotor	0.00625	0.00628	0.00629
Lower rotor	0.00644	0.00648	0.00649
Total rotors	0.01269	0.01276	0.01278

Table 7: Comparison of averaged thrust coefficient of total rotors on IRS in low and high-speed conditions

IRS	0.055	0.083	0.110
μ=0.15	0.01460	0.01487	0.01513
Growth rate	-	+1.85%	+3.63%
μ=0.41	0.01269	0.01276	0.01278
Growth rate	-	+0.56%	+0.71%

The IRS effect on the normal force on the blade's spanwise in high-speed flight conditions is shown in Figure 17. The DBLN-526 airfoil provides minimal changes in normal force before to the chord location 0.331R, similar to low-speed flight conditions, though the IRS increases. However, there was a significant change in normal force for the chord position range of 0.6R to the tip when employing the SSCA-09 airfoil. When IRS increases, the upper rotor indicates an increase in normal force towards the blade's tip, while the lower rotor shows a decrease. To explain these results, one needs to investigate the normal forces generated on the blade's chord at an azimuth angle at a chord position of 0.85R or the same location as the investigation in low-speed flight conditions.

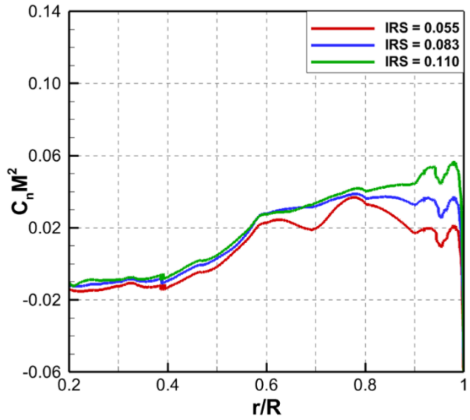

(a) Upper rotor (CCW)

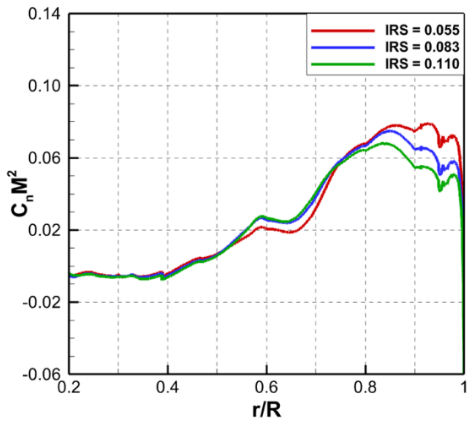

(b) Lower rotor (CW)

Figure 17: Normal force coefficient of rotor blade on spanwise in high-speed flight condition

Figure 18 displays the IRS effects on the normal force at the chord location of 0.85R in high-speed flight conditions on the azimuth angle. The smallest IRS showed the largest fluctuation amplitude at the upper rotor in the high relative speed area with the azimuth angle from 0° to 180°, and the lower rotor from 180° to 360°. Regardless of the azimuth angle, the normal force was similarly analyzed in all ranges while the IRS increased. The reduced wake absorption from the lower rotor and the decreased interference between the upper rotor's wake and the lower rotor as the separation distance increased led to a reduction in the amplitude of normal force fluctuations with increasing IRS. However, the thrust increaseing rate with IRS is less in high-speed flight conditions than in low-speed flight conditions.

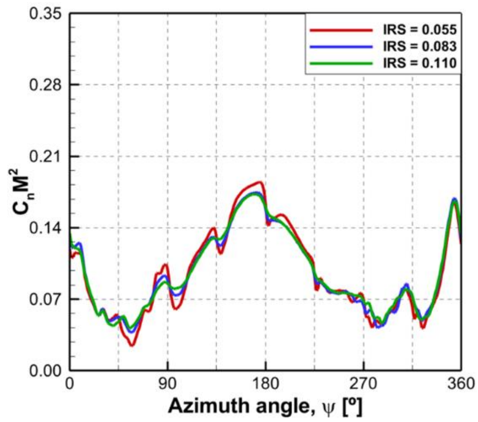

(a) Upper rotor (CCW)

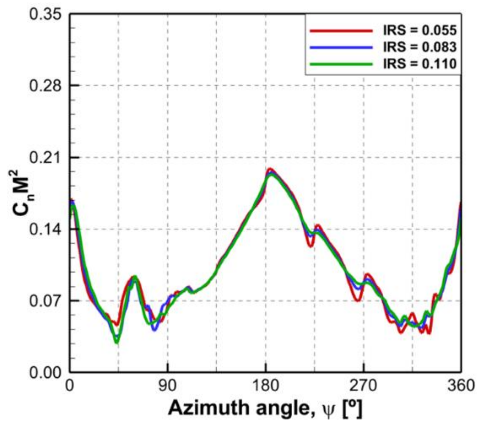

(b) Lower rotor (CW)

Figure 18: Sectional normal force coefficient on azimuth angle at r/R=0.85 in high-speed flight condition

To analyze the IRS effects on the coaxial rotor helicopter's wake structure, Figure 19 displays how IRS affects the wake characteristics in high-speed flight conditions using Q-criterion Iso-surface. While the IRS increases, the vorticity intensity at the advancing and retreating sides of the rotor blades is unchanged, in contrast to low-speed conditions. Furthermore, the turbulence around the rotor blades gets weakened because of the fast-forward flight, even though there was little interference between the

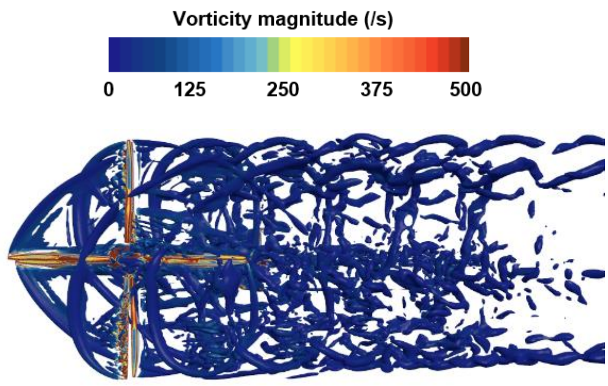

(a) IRS = 0.055

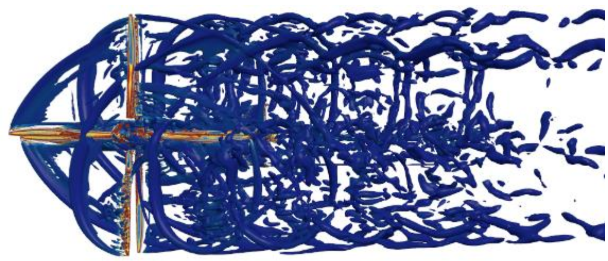

(b) IRS = 0.083

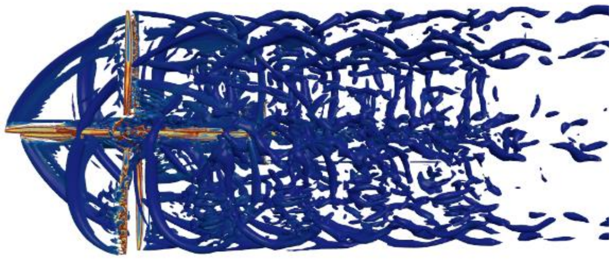

(c) IRS = 0.110

Figure 19: Wake structures represented by an iso-surface of Q-criterion colored by vorticity magnitude in high-speed flight condition

wakes produced by the upper and lower rotor blades.

Figure 20 analyzes the IRS effects on the flow, which could interfere with the fuselage in high-speed flight conditions using the vorticity field. Interference between the wakes generated by the upper and lower rotors is visible in Figure 20(a), but it's not as much as in low-speed flight conditions. So, the only flow with weak vorticity propagates toward the rear side. Small-scale vortices were created when the IRS increased, as shown in Figure 20(b) and Figure 20(c), and the interference between the wakes and the fuselage is almost nonexistent. IRS effects on the fuselage's pitching moment in high-speed flight conditions on azimuth angle are shown in Figure 21. It also indicates 8/rev fluctuations, the same as low-speed flight conditions.

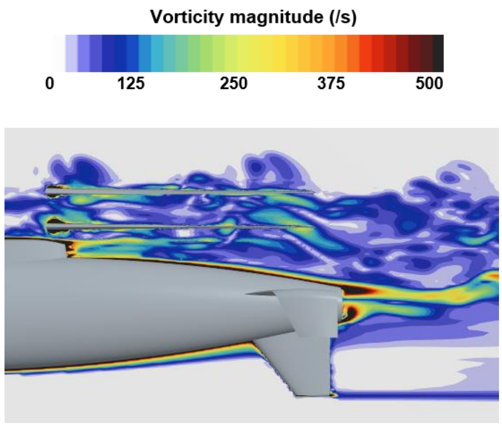

(a) IRS = 0.055

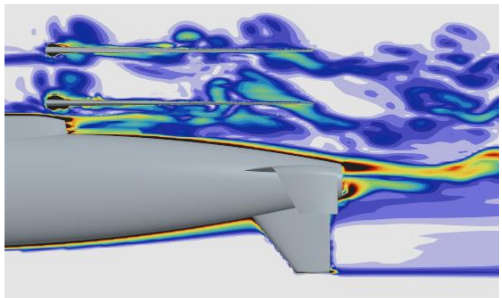

(b) IRS = 0.083

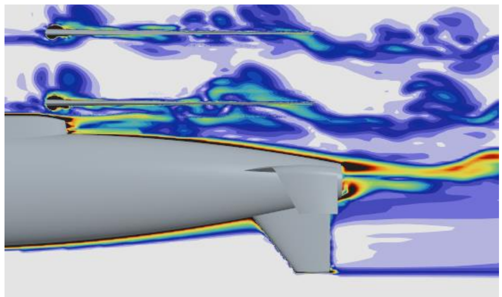

(c) IRS = 0.110

Figure 20: Vorticity contours around X2TD helicopter with IRS effect in high-speed flight condition

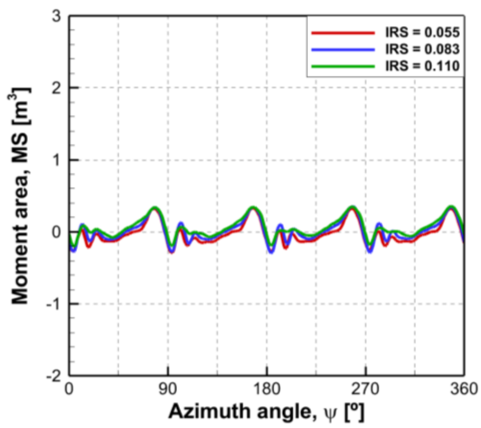

Figure 21: Moment area of the fuselage at IRS effect on azimuth angle in high-speed flight condition

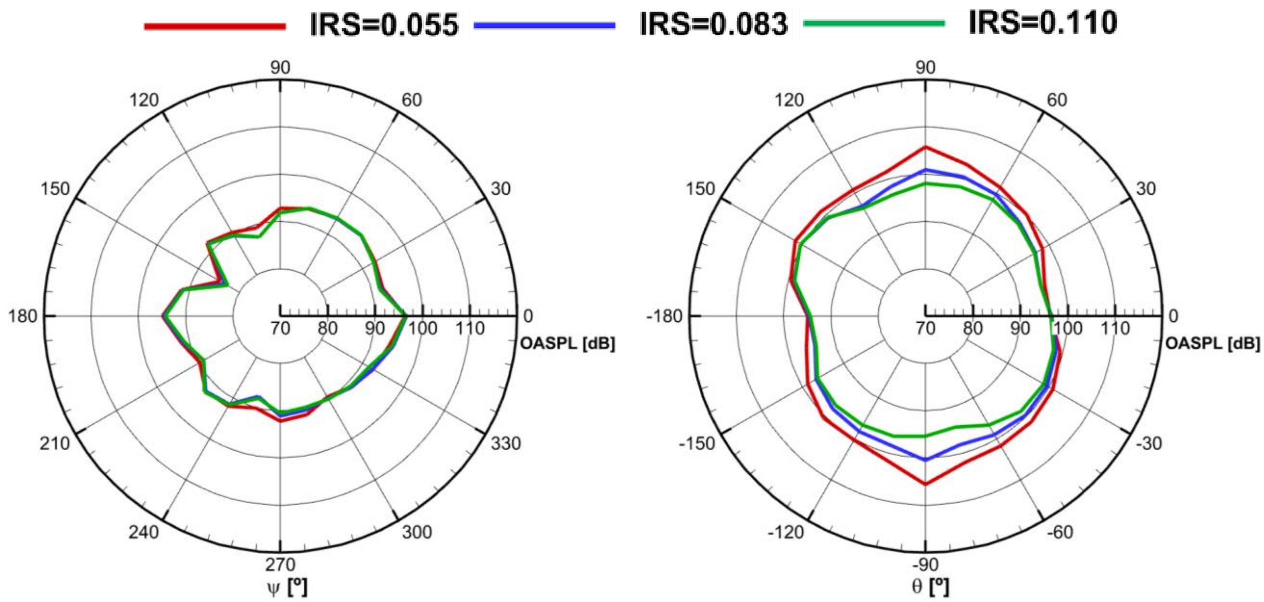

(a) Azimuth angle (b) Elevation angle

Figure 22: Variation of Overall Sound Pressure Level (OASPL) in low-speed flight condition

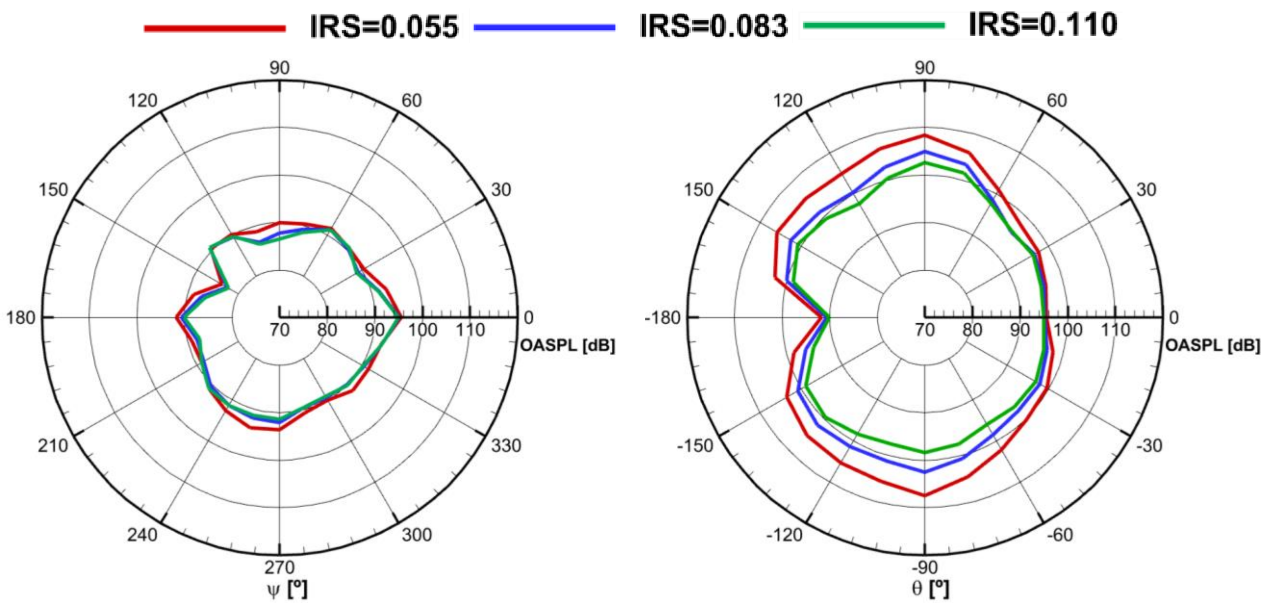

(a) Azimuth angle (b) Elevation angle

Figure 23: Variation of Overall Sound Pressure Level (OASPL) in high-speed flight condition

However, because the interference scale between the wake and the fuselage is smaller, the IRS changes hardly affect the fuselage's pitching moment. So, although the IRS increases, the maneuverability will not be changed.

5.4. IRS Effects on Noise of Coaxial Rotor Helicopter

The IRS effects in low and high-speed flight conditions significantly affect the aerodynamics of a coaxial rotor helicopter, which could impact its aeroacoustic performance. Figure 22 and Figure 23

Analyze the IRS effects on the X2TD helicopter's aeroacoustics by investigating the Overall Sound Pressure Level (OASPL) across the azimuth and elevation angles in low and high-speed flight conditions. At the azimuth angle, noise levels decrease with increasing IRS, mainly due to reduced thickness noise on the advancing and retreating sides of the rotor blades. In low-speed flight conditions,

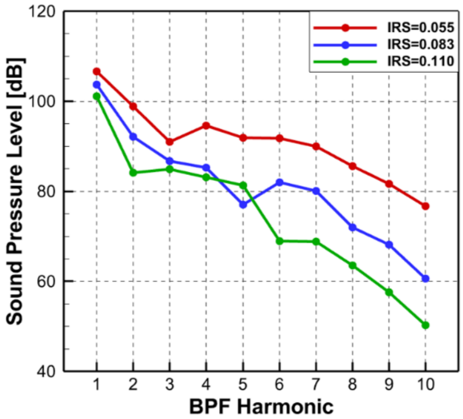

(a) θ = 90°

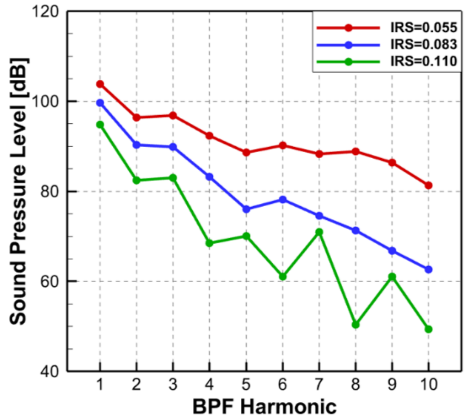

(b) θ = -90°

Figure 24: Comparison of acoustic BPF harmonic spectra in low-speed flight condition

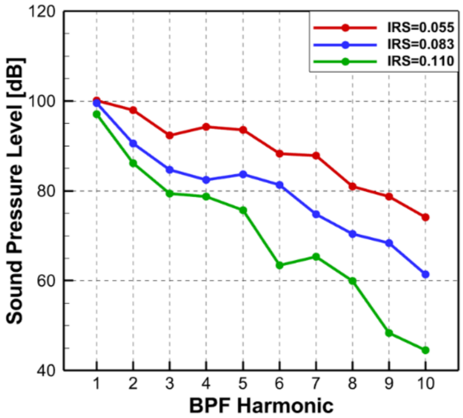

(a) θ = 90°

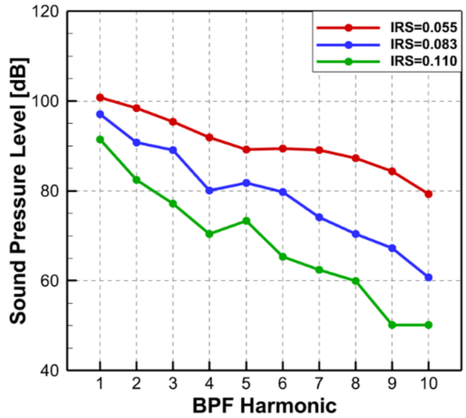

(b) θ = -90°

Figure 25: Comparison of acoustic BPF harmonic spectra in high-speed flight condition

noise levels at IRS=0.083 and IRS=0.10 were about 2 dB lower than IRS=0.055. Looking at high-speed flight conditions, the case of IRS=0.083 created noise 2 dB lower than IRS=0.055, and the IRS=0.110 reduced an additional 1 dB. Also, noise levels decreased with increasing IRS at the elevation angle, especially at 90° and -90°, where the reductions were the most noticeable. Specifically, at 90°, the case of IRS=0.083 predicted 4 dB lower noise than at IRS=0.055, and the case of IRS=0.110 reduced by 6 dB. At -90°, the noise reductions were 5 dB and 7 dB in the cases of IRS=0.083 and IRS=0.110, respectively. These indicate that increasing IRS reduces the interference between the rotor wakes and between the rotors and the fuselage, decreasing the unsteady loading noise. This reduction is particularly significant at elevation angles of 90° and -90°, so it is essential to analyze the noise specifically in these areas through the BPF harmonic spectra To investigate significant noise differences, Figure 24 and Figure 25 demonstrate the IRS effects on the BPF harmonic spectra at elevation angles of 90° and -90° in both low-speed and high-speed flight conditions. The first BPF showed a reduction in noise

of about 0.5 dB for IRS=0.083 compared to IRS=0.055 and a decrease of 3 dB for IRS=0.110 in the low-speed flight condition at an elevation angle of 90°. It shows that at -90°, the noises were predicted 4 and 9 dB lower than for the IRS=0.055 case. Subsequent BPFs showed a general decrease in noise levels with increasing IRS. The first BPF in the high-speed flight condition depicted noise reductions of 3 dB and 5 dB with increasing IRS at 90°, with noise reductions of 4 dB and 9 dB at -90°. The investigation of the contributions of helicopter components to the noise when IRS changes are required by a more significant decrease in noise at -90° than at 90°. At

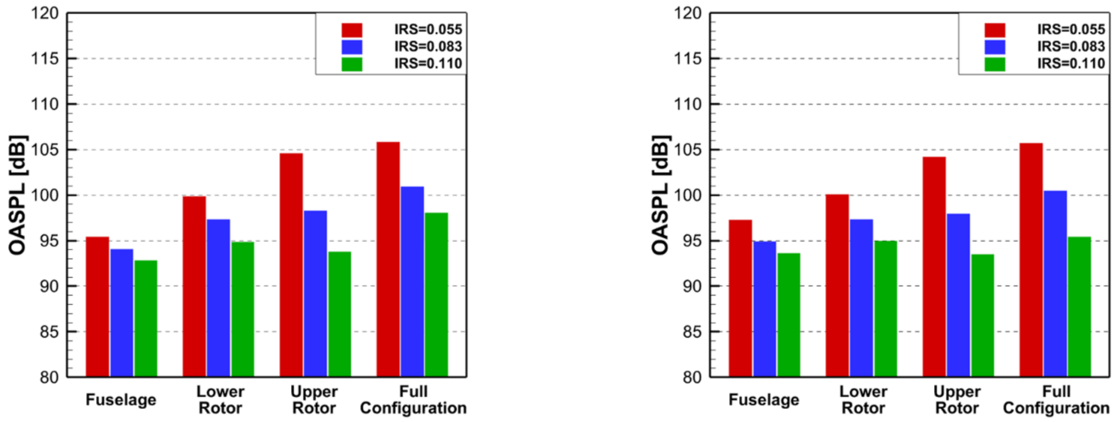

(a) θ = 90°   (b) θ = -90°

Figure 26: Comparison of noise contribution at different elevation angles in low-speed flight condition

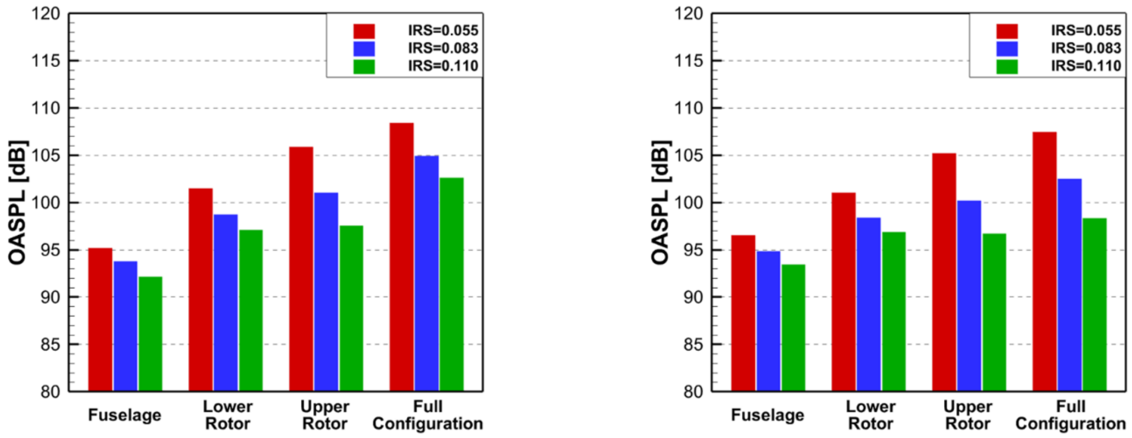

(a) θ = 90°   (b) θ = -90°

Figure 27: Comparison of noise contribution at different elevation angles in high-speed flight condition

elevation angles of 90° and -90°, Figures 26 and Figure 27 demonstrate the noise contribution from the X2TD helicopter's upper and lower rotors, fuselage, and full configuration as IRS changes. The upper rotor was shown to be the main source of noises affecting the acoustics of the helicopter, while the fuselage has the most minor effect on noise levels in all conditions. In both low and high-speed flight conditions, the noise produced by the fuselage decreased by 1 dB at 90° and 2 dB and 3 dB at -90°, respectively, when IRS increased from the case of IRS=0.055 to IRS=0.083 and IRS=0.110. For the upper rotor, in low-speed flight conditions, noise decreased by 6 dB and 11 dB at 90° and -90°, respectively, as IRS increased. And in high-speed flight conditions, lower noises were predicted by 5 dB and 8 dB, respectively. Consequently, for both conditions, the noise created from the full configuration decreased by 5 dB when IRS increased from IIRS=0.055 to IRS=0.083 and by 7 dB in the case of IRS=0.110 at 90°. At -90° location, noise decreased by 5 dB at IRS=0.083 and by 10 dB at IRS=0.110. This demonstrates a reduction in noise contribution from the upper rotor, leading to lower noise levels in the full configuration under both conditions.

6. CONCLUSIONS

This study employed the SA-DES governing equations and the FW-H acoustic analogy method to analyze and compare the noise and aerodynamic effects of IRS on the coaxial rotor at the main rotors of the high-speed and long-range compound helicopter X2TD in low-speed conditions with an advance ratio of 0.15 and high-speed conditions with an advance ratio of 0.41. Based on the advance ratio, the thrust and power of the coaxial rotor model Harrington rotor 1 in forward flight were investigated and compared with experimental data. This study compared the X2TD rotor's normal forces, which depend on azimuth angle and advance ratio, with other computational results. The thrust created by the blades and the normal forces on the spanwise and azimuth angles all showed aerodynamic effects due to IRS. Pitching moments resulting from the fuselage through vortex flow fields were compared. Noise at elevation angles was examined to investigate the IRS effect on loading noise. The effects of IRS changes on noise and aerodynamics at low-speed and high-speed conditions are discussed below.

1. In low-speed conditions, as IRS increases, the strength of the lower rotor to absorb the wake from the upper rotor weakens, and the interference between the wake generated by the upper and lower rotors decreases, resulting in increased thrust and a reduction in the amplitude of thrust fluctuations on the azimuth angle. In high-speed conditions, even though IRS increases, the wakes generated by the two rotors propagate faster than in low-speed conditions, resulting in a lower rate of increase in thrust.
2. Strong rolled-up phenomena and significant vorticity are created at the advancing and retreating sides of the blades when low-speed conditions with low IRS go on due to the overlapping of the wakes from the upper and lower rotors. As IRS increases, the interference between these two wakes becomes weaker. However, in high-speed conditions, the two rotors' wakes propagate faster in the direction of the rear, reducing the effect of IRS on wake interference.
3. Aerodynamic interference occurs when the two rotors' wakes flow toward the fuselage's horizontal stabilizer during forward flight. At low-speed conditions, this interference diminishes with increasing IRS, reducing the fuselage's pitching moment. Even when the IRS grows, the impact on the fuselage's pitching moment is minimal because, in high-speed conditions, the wake generated by the upper rotor and the fuselage almost rarely interact.
4. Noise reduction over a range of angles results from less loading noise affecting the upper and lower rotors as the IRS increases, both in low-speed and high-speed conditions
5. The hub in the main rotor of a coaxial rotor-based helicopter generates most of the drag in the full configuration of the helicopter. When the IRS increases, the size of the mast fairing located between the upper and lower rotors also increases, potentially generating detrimental drag. Therefore, the impact of IRS on the drag will be analyzed for coaxial rotor-based helicopters equipped with a hub and mast fairing.

Author contact:

Sung-U Kang kadough@gnu.ac.kr

Si-Jin Kim eunmin9707@gnu.ac.kr

Kyu-Tae Park kyutae980416@gnu.ac.kr

Seong Jin Jo tjdwls0045@gnu.ac.kr

Rho shin Myong myong@gnu.ac.kr

Hakjin Lee hlee@gnu.ac.kr

6. ACKNOWLEDGMENTS

This study was supported by Korea Research Institute for defense Technology planning and ad-vancement(KRIT) grant funded by the Korea gov-ernment(Defense Acquisition Program Ad-ministration; DAPA) (KRIT-CT-23-010, VTOL Technology Research Center for Defense Applications 2024-contribution 80%) This work was supported by the National Research Foundation of Korea (NRF) grant funded by the Korea government (MSIT) (RS-2024-00397400-contribution 20%)

7. REFERENCES

1. Bagai, A., "Aerodynamic Design of the X2 Technology Demonstrator™ Main Rotor Blade," Annual forum proceedings American Helicopter Society, Vol. 64, (1), 2008.
2. Ventura Diaz, P., Caracuel Rubio, R., and Yoon, S., "Simulations of ducted and coaxial rotors for air taxi operations," AIAA Aviation 2019 Forum, 2019, p. 2825.
3. Pradeep, P., and Wei, P., "Energy-Efficient Arrival with RTA Constraint for Multirotor EVTOL in Urban Air Mobility," Journal of Aerospace Information Systems, Vol. 16, (7), 2019, pp. 263-277. DOI: 10.2514/1.I010710.
4. Denton, H., and Benedict, M., "Investigation of Coaxial Rotor Performance for a Gun-launched Micro Air Vehicle," Vertical Flight Society's 79th Annual Forum & Technology Display, West Palm Beach, FL., USA, May 16-18. 2023. DOI: 10.4050/F-0079-2023-17961.
5. Coleman, C. P., "A Survey of Theoretical and

Experimental Coaxial Rotor Aerodynamic Research," NASA TP 3675, Washington, DC, 1997.
6. Ramasamy, M., "Hover Performance Measurements Toward Understanding Aerodynamic Interference in Coaxial Compound Helicopters," Journal of Aircraft, Vol. 56, (3), 2015, pp. 1-17. DOI: 10.4050/JAHS.60.032005.
7. Yuan, Y., Chen, R., and Li, Pi., "Trim Investigation for Coaxial Rigid Rotor Helicopters Using and Improved Aerodynamic Interference Model," Aerospace Science and Technology, Vol. 85, 2019, pp. 293-304. DOI: 10.1016/j.ast.2018.11.044.
8. Jia, Z., and Lee, S., "Impulsive Loading Noise of a Lift-Offset Coaxial Rotor in High-Speed Forward Flight," AIAA Journal, Vol. 58, (2), 2020, pp. 687-701. DOI: 10.2514/1.J058295.
9. Leishman, J. G., and Anathan, S., "An Optimum Coaxial Rotor System for Axial Flight," Journal of the American Helicopter Society, Vol. 53, (4), 2008, pp. 366-381, DOI: 10.4050/JAHS.53.366.
10. Lee, S. and Dassonville, M., "Iterative Blade Element Momentum Theory for Predicting Coaxial Rotor Performance in Hover," Journal of the American Helicopter Society, Vol. 65, (4), 2020, pp. 1-12. DOI: 10.4050/JAHS.65.042005.
11. Harrington, R.D., "Full-scale-Tunnel Investigation of the Static-Thrust Performance of a Coaxial Helicopter Rotor," NACA TN-2318, 1951.
12. Leishman, J.G., and Syal, M., "Figure of Merit Definition for Coaxial Rotors," Journal of the American Helicopter Society, Vol. 53, (3), 2008, pp. 290-300. DOI: 10.4050/JAHS.53.290.
13. Ho, J.C., Yeo, H., and Bhagwat, M., "Validation of Rotorcraft Comprehensive Analysis Performance Predictions for Coaxial Rotors in Hover," Journal of the American Helicopter Society, Vol. 62, (2), 2017, pp.1-13. DOI: 10.4050/JAHS.62.022005.
14. Nagashima, T., and Nakanishi, K., "Optimum Performance and Wake Geometry of Coaxial Rotor in Hover," Aeronautical and Space Sciences Japan, Vol. 26, (293), 1978, pp.325-333. DOI: 10.2322/jjass1969.26.325.
15. Ko, J. and Lee, S., "Numerical Investigation of Inter-Rotor Spacing Effects on Wake Dynamics of Coaxial Rotors," Journal of Aircraft, Vol. 58, (2), 2020, pp. 363-373. DOI: 10.2514/1.C035857.
16. Qi, H., Xu, G., Lu, C., and Shi, Y., "A Study of Coaxial Rotor Aerodynamic Interaction Mechanism in Hover with High-Efficient Trim Model," Aerospace Science and Technology, Vol. 84, 2019, pp. 1116-1130. DOI: 10.1016/j.ast.2018.11.053.
17. Park, S. H., and Kwon, O. J., "Numerical Study about Aerodynamic Interaction for Coaxial Rotor Blades," International Journal of Aeronautical and Space Sciences, Vol. 22, (2), 2021, pp. 277-286. DOI: 10.1007/s42405-020-00310-6.
18. Chaderjian, N. M., "Advances in Rotor Performances and Turbulent Wake Simulation Using DES and Adaptive Mesh Refinement," 7th International Conference on Computational Fluid Dynamics, Big Island, Hawaii, July 2012.
19. Xu, H. Y., and Ye, Z., Y., "Coaxial Rotor Helicopter in Hover Based on Unstructured Dynamic Overset Grids," Journal of Aircraft, Vol. 47, (5), 2010. pp. 1820-1824. DOI: 10.2514/1.C031079.
20. Breuer, M., Jovičić, N., and Mazaev, K., "Comparison of DES, RANS, and LES for the Separated Flow around a Flat Plate at High Incidence," International Journal for Numerical Methods in Fluids, Vol. 4, (3), 2003, pp. 357-388. DOI: 10.1002/fld.445.
21. Lee, H., and Lee, D. J., "Prediction of Aerodynamic Noise Radiated from a Small Multicopter Unmanned Aerial Vehicle using Acoustic Analogy," Transactions of the Korean Society for Noise and Vibration Engineering, Vol. 29, (4), 2019, pp. 518-526. DOI: 10.5050/KSNVE.2019.29.4.518.
22. Kim, E. M., Yang, J. Y., Lee, H. J., Kang, M. J.,

Myong, R. S., and Lee, H., “Numerical Prediction of Rotor-Airframe Interaction Noise,” Journal of Computational Fluids Engineering, Vol. 27, (3), 2022, pp. 79-88. DOI: 10.6112/kscfe.2022.27.3.079.

23. Kim, E. M., Yang, J. Y., Lee, H. J., Kang, M. J., Myong, R. S., and Lee, H., “Computational Investigation of Airframe Shape Effect on Rotor-Airframe Interaction Noise,” Journal of Computational Fluids Engineering, Vol. 28, (1), 2023, pp. 103-113. DOI: 10.6112/kscfe.2022.27.3.079.
24. Passe, B. J., Sridharan, A., and Baeder, J., “Computational Investigation of Coaxial Rotor Interactional Aerodynamics in Steady Forward Flight,” 33rd AIAA Aerodynamics Conference, 2015.
25. Walsh, D., Weiner, S., Arifian, K., Lawrence, T., Wilson, M., and Blackwell, R., “Development Testing of the Sikorsky X2 TechnologyTM Demonstrator,” 67th Annual Forum of the American Helicopter Society International, Virginia Beach, VA, May 2011.
26. Bagai, A., “Aerodynamic Design of the X2 Technology DemonstratorTM Main Rotor Blade,” 64th Annual Forum of the American Helicopter Society International, Montreal Canada, April 29-May 1, 2008.
27. Barbely, N. L., and Komerath, N. M., “Coaxial Rotor Flow Phenomena in Forward Flight,” 2016 International Powered Lift Conference (IPLC)/SAE Aerospace Sytems and Technology Conference, No. ARC-E-DAA-TN31139, 2016.
28. Linton, D., Widjaja, R., and Thornber, B., “Simulations of Tandem and Coaxial Rotors using a CFD-coupled Rotor Model,” 21st Australasian Fluid Mechanics Conference, December, 2018.
29. Yoon, S., Chan, M. W., and Pulliam, T. H., “Computations of Torque-Balanced Coaxial Rotor Flows,” 55th AIAA Aerospace Sciences Meeting, Grapevine, Texas, January, 2017. DOI: 10.2514/6.2017-0052.